Cosmic telescope chromacity: apparent spectral distortions in a high-redshift, gravitationally lensed starburst/AGN

Roger P. Deane

Astrophysics, Cosmology and Gravity Centre, Department of Astronomy, University of Cape Town, Private Bag X3, Rondebosch 7701, South Africa

E-mail: roger.deane@ast.uct.ac.za

Abstract. Strong gravitational lensing provides us with our deepest views of high-redshift galaxies, the effective sensitivity and angular resolution of which will only be possible with next-generation facilities for unlensed objects. However, any conclusions based on strong-lensing observations are crucially dependent on the 'calibration' of the cosmic telescope, i.e. the robust derivation of an accurate lens model. I present a new Bayesian Markov Chain Monte Carlo algorithm used to constrain the lens model of the high-redshift source IRAS F10214+47, which is routinely used as an archetype Ultra-Luminous InfraRed Galaxy (ULIRG). Using this new model, in combination with high resolution VLBI, *JVLA* CO (1-0) and *HST* optical/ultraviolet observations, the level of effective chromacity is constrained. This is the apparent distortion of the global spectral energy distribution (SED), owing to different emission components undergoing differing magnification boosts by virtue of their relative size and proximity to the lensing caustic. I argue that emission associated with the active nucleus in IRAS F10214+47 is preferentially magnified by an order of magnitude above that of emission associated with star formation, a model which explains a number of peculiarities of this famous galaxy. The demonstration of this spectral distortion by strong-lensing raises caution in the use of any lensed objects as archetypical sources; as well as statistical conclusions based on samples without accurate lens models.

1. Introduction

Over the past 15 years, both theory and observations have shown that star formation and the growth of super-massive black holes in galaxies are fundamentally linked [1, 2, 3, 4]. However, the physical mechanisms that drive the strong correlations of black hole mass ($M_{\rm BH}$) with both the stellar bulge mass ($M_{\rm bulge}$) and stellar velocity dispersion ($\sigma^{\star}$) are not yet clearly understood. Detailed observations of galaxies at cosmological distances play an essential part in the refinement of our theoretical and subsequent numerical models of galaxy evolution over cosmic time. High spatial resolution observations of galaxies with both starburst and AGN characteristics are able to give a unique perspective of the interplay of these components. This is a particularly powerful probe of galaxy evolution at z$\sim$2, corresponding to the peak of quasar and star formation activity [5, 6]. However, detailed, high resolution studies of galaxies at this epoch are challenging as the imaging and 2D-spectral requirements are close to the limits of current instrumentation. To this end, many observations target gravitationally lensed sources which undergo a natural boost in flux and angular extent. A source magnification of μ saves a factor

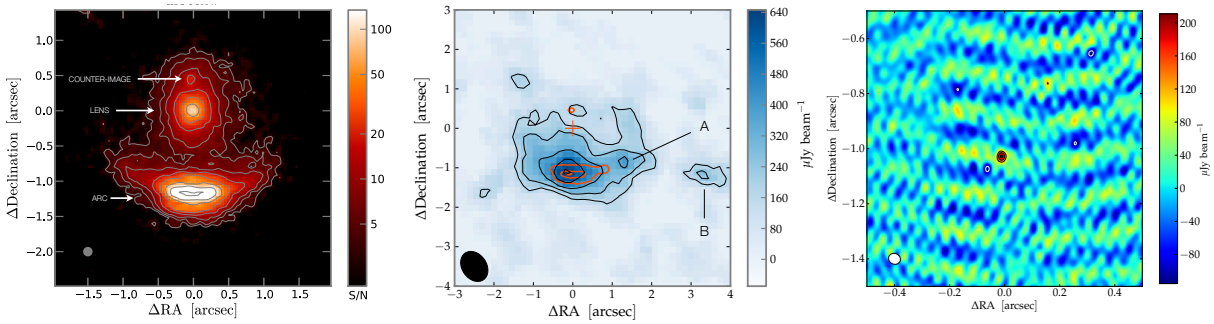

Figure 1. **Left:** *HST* F160W map with lensing galaxy, counter-image and the arc. **Middle:** CO (1→0) intensity map with *HST* rest-frame ultraviolet contours overlaid in red and the centroid of the lens galaxy is indicated with a red cross. The CO (1→0) contours (black) are at 2-σ intervals and start at -3, 3-σ where $\sigma = 60\ \mu$Jy beam^{-1}. **Right:** EVN 1.66 GHz continuum map with contours starting from -4, 4-σ and increasing in steps of 2-σ, where $\sigma = 23\ \mu$Jy per beam. The observed noise structure results from the *EVN* synthesised beam. The map co-ordinates are centred on the lensing galaxy *HST* F160W centroid (RA = $10^{\rm h}\ 24^{\rm m}\ 34.5622^{\rm s}$, Dec = 47° 09' 10.809", see **D12a**). The PSFs of the colour-scale maps shown above are all indicated in the bottom left of each frame and have FWHM of $\theta_{\rm PSF}$ ∼0.15 arcsec; 0.7 arcsec; and 0.042 arcsec for the *HST*, *JVLA* and *EVN* respectively.

μ^2 in observation time to achieve the equivalent sensitivity, making these 'cosmic telescopes' powerful tools in high-redshift astrophysics *provided that* accurate lens models are derived.

Although gravitational lensing is achromatic, different emission scales have differing magnification factors that can result in a distortion of the global spectral energy distribution (SED). This SED distortion is usually ignored or not quantified in studies that use lensing as a comic telescope to investigate the background source, especially in the (sub)millimetre regime where spatial resolution is poor and/or multiple images are not detected and able to constrain the lens model. This contribution presents a subset of results from an extensive radio/mm observing programme to quantify this effect and the intrinsic starburst/AGN energy contributions in the famous strongly lensed system IRAS FSC10214+47 (IRAS 10214 hereafter).

In the following, I focus on the main AGN and star formation proxies (the VLBI-detected core and spatially-resolved CO (1→0)), as well as the *HST* maps to compare the host galaxy (old stellar component) and narrow-line region properties. The aim is to derive the true magnification (and hence size) as well as the source-plane position, in order to reconstruct the intrinsic properties of IRAS 10214. I refer extensively to work reported in Deane et al. (2012a,b,c), denoted **D12a**, **D12b**, and **D12c** hereafter.

2. Observations

2.1. HST F160W

The *HST* F160W map is shown in Fig. 2.1 (left) and shows a strong arc structure, the lens as well as a counter-image to the north of the lens. This filter appears to be dominated by the host galaxy (i.e. the older stellar component) based on the global SED (see **D12a**) as well as the 4000 Å break first identified by [7]. The source plane properties of the *HST* F160W map are explored in Deane et al. (2012d, in prep.).

2.2. HST F814W

This rest-frame ultraviolet map was the first conclusive evidence that IRAS 10214 is indeed gravitationally lensed. The morphology (see red contours in Fig. 2.1, middle) shows a clear ∼1 arcsec long arc and a low S/N detection of the counter-image. The lensing galaxy has been subtracted using a GALFIT 3 [8] Sersic fit. The observations, derived properties and lens modelling are fully described in [9]. Since this is the map we use for the lens model derivation, two key attributes are accurate point spread function (PSF) characterisation and astrometry. The PSF FWHM is ∼100 mas as derived from the 'Tiny Tim' *HST* software package using a K-star source colour since an accurate empirical estimate was not possible. This is fully

described in [9] and is consistent with two stars in the field, one of which is saturated and the other too weak for accurate PSF estimation. As with the *HST* F160W map, the astrometry is in agreement with determinations from [10, 9, 11] and Simpson et al. (2012, in prep) to within $\Delta\theta < 10$ mas.

2.3. JVLA CO(1-0)

We observed the CO (1→0) rotational line, redshifted to $\nu_{\rm obs} = 35.08376$ GHz, toward IRAS 10214 using the *JVLA* (C configuration) in October 2010. All data reduction was performed using standard reduction techniques in *AIPS*, which are fully described in **D12b**. All maps were generated with natural weighting yielding a synthesised beam size $\theta_{\rm syn} \sim 0.82 \times 0.62$ arcsec^2. The integrated intensity map is shown in Fig. 2.1 and reveals a clearly extended morphology, particularly in the east-west direction which spans ~ 3.5 arcsec. An 'arc-like' structure is observed, and this is clearer still in a few of the channel maps. The peak of the CO (1→0) total intensity map is co-spatial with the *Hubble Space Telescope (HST)* rest-frame UV map. Accounting for the lower spatial resolution of this map, the source is significantly more extended in CO (1→0) than the optical, near-infrared and radio components presented in **D12a**.

2.4. VLBI 1.7 GHz

Observations of IRAS 10214 were made with the *European VLBI Network* (*EVN*) at 1.66 GHz on 2 and 3 November 2010. Stations that were used in these observations included Jodrell Bank (76-metre), Westerbork Radio Synthesis Array (WRST, phased array), Effelsberg, Onsala (26-metre), Medicina, Torun, Cambridge, Knockin, as well as the three Russian out-stations: Svetloe, Zelenchuk and Badary. This resulted in a baseline coverage of roughly 100 km to 5000 km, corresponding to an angular scale range of 500 mas to 10 mas at an observing frequency of 1.66 GHz. It is for this reason that VLBI observations apply a brightness temperature filter which enables the unambiguous determination of the active core radio flux - one of the primary aims of this work. The full observational strategy and calibration techniques are extensive and detailed in **D12c**. In Fig. 2.1 (right) we show the *EVN* 1.66 GHz CLEANED map with a 9-σ detection. The peak flux density of the imaged data is $S_{\rm peak} = 209 \pm 23$ μJy. Fitting a Gaussian to the CLEANED map returns an integrated flux density $S_{\rm int} = 220 \pm 37$ μJy, which suggests that the source is unresolved. The positional uncertainty is $\sigma_\theta = 2.2$ mas, which is defined by $\sigma_\theta = 0.5\,{\rm FWHM}/({\rm S/N})$ [12].

The *EVN* detection lies roughly halfway along the main *HST* F814W arc (in RA), and > 100 mas northward of the centre of curvature. It is located ∼170 mas towards the north-west of the main (eastern) *HST* F814W peak. The radio coordinate reference frame is directly compared to the optical reference frame in [13] who find no offset.

3. Lens Modelling

Gravitational lensing occurs as a result of the apparent deflection of light between the astrophysical source and observer by an intervening mass that curves the local spacetime. The gravitational lensing formalism is comprehensively covered in many texts (e.g. [14]) and therefore, in the interests of brevity, is not repeated here. The lens modelling algorithm is detailed in **D12a**, however we provide a brief overview here.

We derive the lens model parameters, given the data which are the *HST* F814W map pixel values. We predict data pixel values which are derived by forward ray-tracing trial source models into the image plane based on a trial lens model. We have developed software that implements a MCMC routine to compare ray-traced trial models to the data and so sample the posterior probability distribution function (PDF) of all free parameters.

Our most successful lens model comprises of the main lens Singular Isothermal Ellipsoid (SIE) potential as well as a Singular Isothermal Sphere (SIS) potential to account for the influence

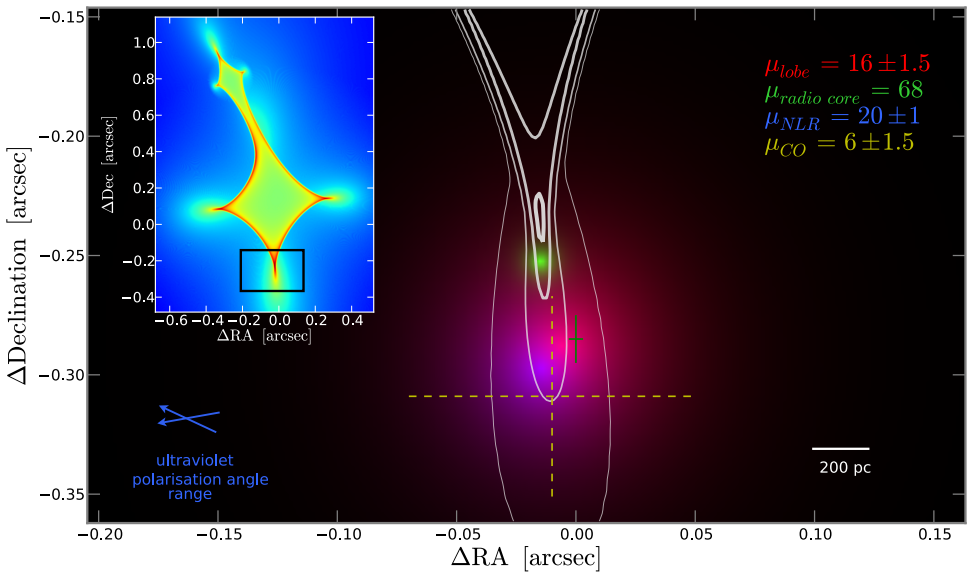

Figure 2. Source plane reconstruction of IRAS 10214 with AGN core (*EVN* 1.6 GHz, green), scattered quasar light (*HST* F814W, blue) and radio lobe (*MERLIN* 1.7 GHz, red). The yellow, dashed cross shows the CO (1→0) total intensity map source plane centroid and its uncertainty (the extent of the source-plane CO (1→0) component is beyond this entire frame). The white contours represent lines of equal magnification extending from the caustic at levels $\mu = 10, 20, 50, 100$. The blue arrows (bottom left) depict the range of ultraviolet polarisation angles along the *HST* F437M arc. The inset shows the full lens caustic with colour-scale representing magnification and the black rectangle showing the borders of the enlarged region.

for the nearby galaxy which is $\Delta\theta$ ~2.2" NNE from the primary lensing galaxy. This results in a model with 7 free parameters: the source's true position and scale radius (x, y, r_s); the main SIE lens Einstein radius, potential ellipticity and position angle $(\theta_E, \varepsilon, PA)$; and finally the neighboring galaxy SIS Einstein radius ($\theta_{E,cmp3}$). The MCMC algorithm is run for 5×10^5 iterations in uncorrelated (eigen-) space to achieve convergence. For further details with regard to the lensing algorithm, and a discussion on the systematic uncertainties, see **D12a**.

4. Source Plane Properties

The source-plane reconstruction of IRAS 10214 is shown in Fig. 2. The AGN and NLR roughly at the centre of the much larger CO (1→0) component. The magnification of the radio core is $\mu_{AGN} = 68$ (modelled as a point source), while the *HST* F814W magnification is $\mu_{NLR} = 20 \pm 1$ (source-plane scale radius $r_{814} = 360$ pc). The source-plane CO (1→0) scale radius $r_{CO} = 5.8 \pm 0.9$ kpc and its overall magnification of $\mu_{CO} = 6 \pm 1.5$ indicates the starburst in this galaxy is significantly less magnified than the AGN and narrow-line region.

The *EVN* source is north-ward of the *HST* arcs and does not split into 3 images (at 4.5-σ significance) and therefore is most likely to the south of (or on) the cusp of the caustic. It is positioned roughly along the vector that extends from the centre of the lens and bisects the angle subtended by the rest-frame UV/optical arcs. This implies that the source-plane position must be very close (< few milli-arcseconds) to the cusp of the caustic, since this is the region with large tangential deflection angles. The *EVN* point source is therefore essentially 'wedged' between the inner-caustic and the *HST* arc, which will always result in high magnifications regardless of changes in the macroscopic lens model.

Assuming the *EVN* point source is the obscured active nucleus, then its source-plane position is consistent with a number of multi-wavelength observations including:

(i) The IRAS 10214 *HST* F437M arc centre-of-curvature is shifted northward (12±14 mas) when compared to that of the *HST* F814W arc (see Fig.1 in [10]). Although the astrometric precision of this measurement is challenging (see [10] for a discussion), the resultant

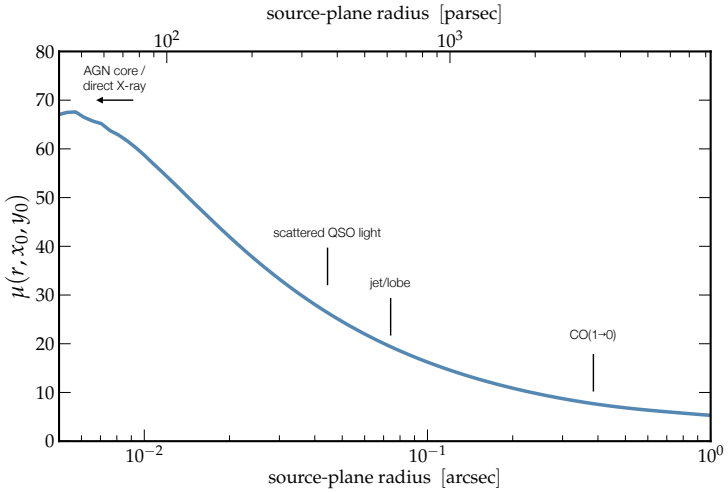

Figure 3. Total magnification as a function of source-plane scale radius, *assuming the EVN source-plane centroid.* The annotations serve as a rough guide of the physical sizes. The centroids of the listed components are not the same as the *EVN* component and therefore the resultant magnifications are different. The point source magnification at the best-fit *EVN* position is $\mu_{\rm pt} = 68$.

interpretation is consistent with a northern AGN core and the fact that shorter wavelengths are scattered more efficiently.

(ii) Simpson et al. (2012, in prep.) present two narrow band maps centred on the redshifted C IV and [O III] lines, which are typical broad-line and narrow-line region emission lines respectively. They determine the centers of curvature of both and find that the C IV is 40 ± 20 mas northward of the [O III] centre of curvature.

(iii) [10] present spatially-resolved polarimetry along the ultraviolet arc of the F437M map which provides an independent test of the source-plane configuration in two forms: the average polarisation angle, as well as its smooth variation along the arc in the *HST* rest-frame UV image. Both the median and flux-weighted mean ultraviolet polarisation angles (from *HST*, *Keck* and *WHT* observations) are consistent with the VLBI core position (see **D12c**).

4.1. Black Hole/Spheroid Mass Ratio

Following the [15] calibration, we determine a black hole mass of $\log_{10}(M_{\rm BH}/{\rm M}_\odot) = 8.36 \pm 0.50$ using the polarised C IV line width. Assuming the *HST* F160W magnification $\mu_{\rm F160W} = 14.1\pm^{1.6}_{1.2}$, we estimate an intrinsic stellar mass of $M_{\rm stellar} = 1.5M^* = 1.5 \times 10^{10.7} = 7 \times 10^9$ M$_\odot$, where the value of $M^* \simeq 10^{10.7}$ M$_\odot$ is the characteristic stellar mass at $z \sim 2$ [16]. We estimate a $M_{\rm BH}/M_{\rm spheroid}$ ratio, where we assume the stellar mass dominates the total spheroid mass inside the $r_{\rm s} \sim 500$ pc source-plane scale radius which is significantly smaller than the CO (1→0) source-plane scale radius ($r_{\rm CO} = 5.7$ kpc) derived in **D12b**. For significantly more detail regarding these calculations, see **D12c**.

The central super-massive black hole to stellar mass ratio, $M_{\rm BH}/M_{\rm stellar} = 0.01$. This value is typically $M_{\rm BH}/M_{\rm spheroid}$ ~0.1-0.2% at $z \sim 0$ [17, 18], but found to increase for high-redshift quasars, albeit with large uncertainty, by a number of authors [19, 20, 21]. Therefore, our derived $M_{\rm BH}/M_{\rm spheroid}$ value is an order of magnitude larger than the typical ratio found at $z \simeq 0$, however consistent with the suggested evolution of this relation for AGN host galaxies. Following [21], we expect an increase in the $M_{\rm BH}/M_{\rm spheroid}$ relation by a factor of $11\pm^{25}_{8}$ at a redshift of $z = 2.3$, in agreement with the our derived values. Although the uncertainties are large, the overall picture strongly supports that the majority of the black hole growth precedes the full stellar mass assembly for this obscured quasar (assuming that IRAS 10214 will evolve

to be consistent with the local $M_{\rm BH}/M_{\rm spheroid}$ relation). This is contrary to the 'under-massive' black holes masses measured in $z \sim 2$ SMGs by [22] and [23].

This tentatively implies very different evolutionary paths for these two object classes, despite their apparent similarities in many parts of the global SED. Selection bias may be at play however, as outlined in [24], particularly since we demonstrate in this work that the AGN is preferentially magnified by an order of magnitude when compared to the spatially resolved *JVLA* CO (1→0) map. For this reason, a significantly enlarged sample size, that has a demonstrably unbiased selection, is required to investigate this further.

5. Conclusions and Future Outlook

Our robust lens model allows a reconstruction of the intrinsic galaxy morphology and properties, accounting for the SED distortion due to the differing magnification factors. The AGN is preferentially magnified by over an order of magnitude when compared to a spatially resolved *JVLA* CO (1→0) map, where the latter can be used as a star formation proxy. This demonstrates the effective 'chromacity' of this strong-lensed system (discussed in **D12a, D12b, D12c**), which is caused by different emission regions undergoing differing magnification boosts due to their relative size and position. This effect may be particularly relevant in the case of far-infrared (FIR) bright strongly-lensed galaxies recently discovered by the *Herschel Space Observatory* [25]. This demonstration of preferential lensing shows that the brightest lenses may be the most affected since the survey selection band is likely to be the very wavelength that is preferentially magnified. This is true in the case in IRAS 10214 which was originally selected at rest-frame $\lambda_{\rm rest} \sim 18$ and 30 μm, which is dominated by preferentially magnified, AGN-heated, hot dust. These results raise caution in the application of statistics derived from strongly-lensed systems without robustly derived lens models. Moreover, the use of IRAS 10214 as a archetype ULIRG is not recommended, unless the significant preferential lensing of the active nucleus is accounted for.

References

[1] Silk, J., & Rees, M. J. 1998, A&A, 331, L1
[2] Magorrian, J., et al. 1998, AJ, 115, 2285
[3] Ferrarese, L., & Merritt, D. 2000, ApJL, 539, L9
[4] Hopkins, P. F., Hernquist, L., Cox, T. J., Di Matteo, T., Robertson, B., & Springel, V. 2006, ApJS, 163, 1
[5] Dunlop, J. S., & Peacock, J. A. 1990, MNRAS, 247, 19
[6] Madau, P., Ferguson, H. C., Dickinson, M. E., Giavalisco, M. et al. 1996, MNRAS, 283, 1388
[7] Lacy, M., Rawlings, S., & Serjeant, S. 1998, MNRAS, 299, 1220
[8] Peng, C. Y., Ho, L. C., Impey, C. D., & Rix, H.-W. 2010, AJ, 139, 2097
[9] Eisenhardt, P. R., Armus, L., Hogg, D. W., Soifer, B. T. et al. 1996, ApJ, 461, 72
[10] Nguyen, H. T., Eisenhardt, P. R., Werner, M. W., Goodrich, R., Hogg, D. W., Armus, L., Soifer, B. T.,
[11] Evans, A. S., Scoville, N. Z., Dinshaw, N., Armus, L., Soifer, B. T. et al. 1999, ApJ, 518, 145
[12] Condon, J. J. 1997, PSPS, 109, 166
[13] Lawrence, A., et al. 1993, MNRAS, 260, 28
[14] Blandford, R. D., & Narayan, R. 1992, ARA&A, 30, 311
[15] Vestergaard, M., & Peterson, B. M. 2006, ApJ, 641, 689
[16] Ilbert, O., et al. 2010, ApJ, 709, 644
[17] Merritt, D., & Ferrarese, L. 2001, MNRAS, 320, L30
[18] Häring, N., & Rix, H.-W. 2004, ApJL, 604, L89
[19] Peng, C. Y., Impey, C. D., Rix, H.-W., Kochanek et al. 2006, ApJ, 649, 616
[20] McLure, R. J., Jarvis, M. J., Targett, T. A., Dunlop, J. S., & Best, P. N. 2006, MNRAS, 368, 1395
[21] Bennert, V. N., Auger, M. W., Treu, T., Woo, J.-H., & Malkan, M. A. 2011, ApJ, 742, 107
[22] Alexander, D. M., et al. 2008, AJ, 135, 1968
[23] Biggs, A. D., Younger, J. D., & Ivison, R. J. 2010, MNRAS, 408, 342
[24] Lauer, T. R., Tremaine, S., Richstone, D., & Faber, S. M. 2007, ApJ, 670, 249
[25] Negrello, M., et al. 2010, Science, 330, 800